Journal of
Manufacturing and Materials Processing

MDPI

Article

Effect of Temperature, Heating Rate, and Cooling Rate on Bonding and Nitriding of AlSi10Mg Powder Occurring During Supersolidus Liquid-Phase Sintering

Alena Kreitcberg [1,*], Mohamed Khaled Trigui [1], Abdelberi Chandoul [1], Roger Pelletier [2] and Vincent Demers [1,*]

[1] Department of Mechanical Engineering, École de Technologie Supérieure, Montréal, QC H3C 1K3, Canada; mohamed-khaled.trigui.1@ens.etsmtl.ca (M.K.T.); abdelberi.chandoul.1@ens.etsmtl.ca (A.C.)
[2] National Research Council of Canada, Boucherville, QC J4B 6G4, Canada; roger.pelletier@cnrc-nrc.gc.ca
* Correspondence: alena.kreitcberg@etsmtl.ca (A.K.); vincent.demers@etsmtl.ca (V.D.); Tel.: +1-514-396-8590 (A.K. & V.D.)

Abstract

This study investigated the effect of supersolidus liquid-phase sintering conditions on the powder particle bonding and the AlN-phase formation of an AlSi10Mg alloy. Sintering was conducted at temperatures between 550 and 579 °C, with a holding duration of 2 h under a nitrogen atmosphere. The sintering cycles included four heating segments, performed at rates ranging from 0.2 to 5 °C/min for a total of between 5 and 15 h, and a cooling segment performed at two different cooling rates, 0.15 and 5 °C/min, resulting in durations of 12 and 70 h, respectively. Three powder batches exhibiting different particle size distributions were tested. An X-ray diffractometer, optical microscopy, and scanning electron microscopy were used to characterize phase formation and particle bonding. The results show that higher sintering temperatures and faster heating/cooling rates led to a lower fraction of AlN. In contrast, lower sintering temperatures or slow heating promoted the development of a thicker AlN shell around powder particles, inhibiting the bonding of the AlSi10Mg powder and preventing densification via the sintering process. These findings suggest that sintering at temperatures between 570 and 575 °C, with heating and cooling rates of at least 2 °C/min, constitutes a more favorable window for the densification of AlSi10Mg under a nitrogen atmosphere.

Keywords: AlSi10Mg alloy; powder; supersolidus liquid-phase sintering; sintering; nitriding; microstructure; fabrication routes

check for updates

Academic Editor: Shuting Lei

Received: 21 July 2025
Revised: 13 August 2025
Accepted: 21 August 2025
Published: 1 September 2025

Citation: Kreitcberg, A.; Trigui, M.K.; Chandoul, A.; Pelletier, R.; Demers, V. Effect of Temperature, Heating Rate, and Cooling Rate on Bonding and Nitriding of AlSi10Mg Powder Occurring During Supersolidus Liquid-Phase Sintering. *J. Manuf. Mater. Process.* **2025**, *9*, 296. https://doi.org/10.3390/jmmp9090296

Copyright: © 2025 by the authors. Licensee MDPI, Basel, Switzerland. This article is an open access article distributed under the terms and conditions of the Creative Commons Attribution (CC BY) license (https://creativecommons.org/licenses/by/4.0/).

1. Introduction

The sintering process begins with direct contact between particles, where mass transport via diffusion drives the formation and growth of sintering necks. This mechanism is predominant during solid-state sintering. However, in the sintering of aluminum, a significant challenge lies in disrupting the highly stable aluminum oxide layer, which acts as a natural barrier to neck formation. Studies reported that the Al_2O_3 layer on bulk aluminum at room temperature typically measures between 1 and 2 nm in thickness, whereas the oxide layer on atomized aluminum powder can range from 5 to 15 nm [1]. Successful sintering requires the disruption of this oxide layer to promote metallic bonding between particles. This can be achieved through mechanical spalling or oxide reduction via the sintering atmosphere or using alloying elements under suitable conditions [2].

The transformation of the oxide layer during sintering contributes to its disruption. The amorphous α-Al_2O_3 layer that forms at room temperature undergoes a phase transformation into γ-Al_2O_3 at temperatures above 400 °C [3]. This transformation induces microcracking within the oxide layer due to differences in the coefficients of thermal expansion (CTE) and density between the α- and γ-Al_2O_3 phases [4]. However, this transformation alone is insufficient to fully disrupt the oxide barrier.

The disparity in CTEs between liquid aluminum and γ-Al_2O_3 is significantly more pronounced, exceeding a twofold difference [5]. The formation of liquid films during sintering, accompanied by localized volume expansion, generates tensile stresses in the oxide layer as the temperature increases, further promoting its disruption [5]. The liquid phase plays a critical role, not only in breaking the oxide layer but also in facilitating neck growth between aluminum particles, promoting powder repacking, and filling interparticle porosity. Together, these processes contribute significantly to the densification of the sintered part [6,7]. To maintain the dimensional stability of the part, a technique known as supersolidus liquid-phase sintering (SLPS) is used. In this approach, the amount of liquid formed during sintering must be carefully controlled, and the sintering temperature should slightly exceed the solidus temperature [8]. However, the non-uniform distribution of the limited fraction of the liquid phase, along with the poor wetting between liquid aluminum and residual Al_2O_3 oxide on unmelted surfaces, can introduce additional challenges [9]. These issues may result in uneven densification and a non-uniform density distribution within the sintered part [10,11].

Moreover, in the presence of oxygen, a new aluminum oxide layer rapidly reforms. To mitigate this, sintering of aluminum powder is typically performed under vacuum or in inert gases such as argon and nitrogen [12]. The presence of magnesium vapor in a nitrogen atmosphere, acting as an oxygen getter, can create a favorable "microclimate" [13]. Indeed, several studies [14–17] suggest that nitrogen transports magnesium vapor throughout the pore network of the debound part, helping in the reduction of the protective Al_2O_3 layer. In aluminum alloys containing Mg, this element can also diffuse to the powder surface and react with Al_2O_3 oxide, forming MgO or $MgAl_2O_4$ spinel, which disrupts and reduces the surface oxide layer [18,19]. Consequently, when present as a vapor or an alloying element (0.1 and 1.0 wt.%), magnesium reduces the oxide layer and exposes the underlying metallic aluminum to the nitrogen atmosphere, where Al and N exothermically react to form AlN [20–23].

The formation of spinels and AlN enhances wettability at the interface between the liquid and solid aluminum phases, thereby promoting densification during sintering [24–26]. For example, the addition of 5 wt.% nano- or submicro-size AlN particles to an AlSi10Mg alloy has been shown to improve densification in laser powder bed fusion (LPBF) additive manufacturing [27]. In contrast, excessive or coarse AlN particles can be detrimental to aluminum alloys. Indeed, the study by [28] indicates that 5 wt.% AlN is optimal for densification in AlSi10Mg powder beds in AM, whereas an increase to 10 wt.% results in poorer densification and lower mechanical properties. However, some studies also suggest that the introduction of silicon into Al-Mg alloys may mitigate oxide reduction and the formation of MgO and $MgAl_2O_4$ films [29], although the underlying mechanisms remain unclear.

AlSi10Mg stands out for its exceptional strength-to-weight ratio, making it highly versatile for aerospace and automotive applications, and it is widely used in both casting and modern laser-based additive-manufacturing (AM) processes such as LPBF [30,31]. Beyond LPBF, this alloy can also be processed using binder jetting (BJ), metal injection molding (MIM), and conventional press-and-sintered powder metallurgy (PM), all alternative techniques requiring a sintering step to promote particle bonding and

densification [32–34]. Unlike the ultrafine, metastable cellular microstructure typically formed in LPBF AlSi10Mg [35], BJ, MIM, and PM processes generally result in a coarser, near-equilibrium microstructure exhibiting lower (or even zero) residual stresses, which may significantly influence the mechanical performance of the final component.

Due to the sufficiently wide temperature gap between its liquidus and solidus, AlSi10Mg is particularly well-suited for SLPS. While sintering behavior has been extensively studied in other aluminum systems [36], the SLPS behavior of AlSi10Mg remains largely unexplored. Furthermore, although studies have shown that direct nitriding of aluminum alloys can occur even at relatively low temperatures [37], the combined effect of sintering conditions and nitriding in AlSi10Mg, especially within or near the SLPS temperature range, has not been previously explored. This study aimed to address this knowledge gap by subjecting AlSi10Mg powder to SLPS under different sintering conditions (including heating rate, holding temperature, and cooling rate) and to investigate the formation of the AlN phase and powder particle bonding during this sintering.

2. Materials and Methods

Three plasma-atomized AlSi10Mg powders with different particle size distributions (PSDs) were used in this study. The first powder lot (AP&C, GE Additive, Saint-Eustache, Canada) was characterized by a wide PSD of 0–110 µm with D_{10}, D_{50}, and D_{90} values of 5, 16, and 42 µm, respectively. The chemical composition of this powder was provided by the manufacturer through its mill certificate and corresponds to the DIN EN 1706 (EN AC—43000) standard [38], as detailed in Table 1.

Table 1. Chemical composition of AlSi10Mg powder (wt. %).

	Al	Si	Mg	Mn	Fe	Ti	Cu	Ni	Zn	Sn	Pb
	Bal.	9–11	0.25–0.45	<0.45	<0.55	<0.15	<0.05	<0.05	<0.1	<0.05	<0.05
Wide-PSD-grade	Bal.	10.3	0.35	<0.01	0.17	0.15	<0.01	<0.01	<0.01	<0.01	<0.01

This wide-PSD powder was sieved to produce one metal injection molding-grade powder (with an MIM grade of 0–20 µm, exhibiting D_{10}, D_{50}, and D_{90} values of 4, 9, and 15 µm) and one binder jetting-grade powder (with a BJ grade of 20–63 µm, exhibiting D_{10}, D_{50}, and D_{90} values of 24, 38, and 55 µm). The PSD results for these three powders are shown in Figure 1, along with representative scanning electron microscope (SEM) micrographs showing a spherical shape with small satellite particles visible on their surfaces.

The partial melting of the powder to form a liquid phase is a key process in SLPS. According to the differential thermal analysis (DTA) measurements shown in Figure 2a, the onset of liquid formation obtained during heating was approximately at 566 °C. The same temperature was also predicted using FactSage 8.4 thermodynamic calculations for AlSi10Mg, based on the chemical composition detailed in Table 1.

The liquid volume fraction was then assessed using the same thermodynamic calculations as a function of temperature, as shown in Figure 2b. However, these calculations assume equilibrium conditions for powder solidification [39]. In practice, atomized powders undergo non-equilibrium solidification, meaning that an equilibrium phase diagram cannot reliably predict the variation in the liquid volume fraction with temperature, but can only be used to define the working window. The sintering process was performed at various temperatures ranging from the solidus to liquidus temperatures (566–579 °C). A sintering temperature of 550 °C was also selected to determine whether sintering in a nitrogen atmosphere is possible at temperatures below the solidus temperature.

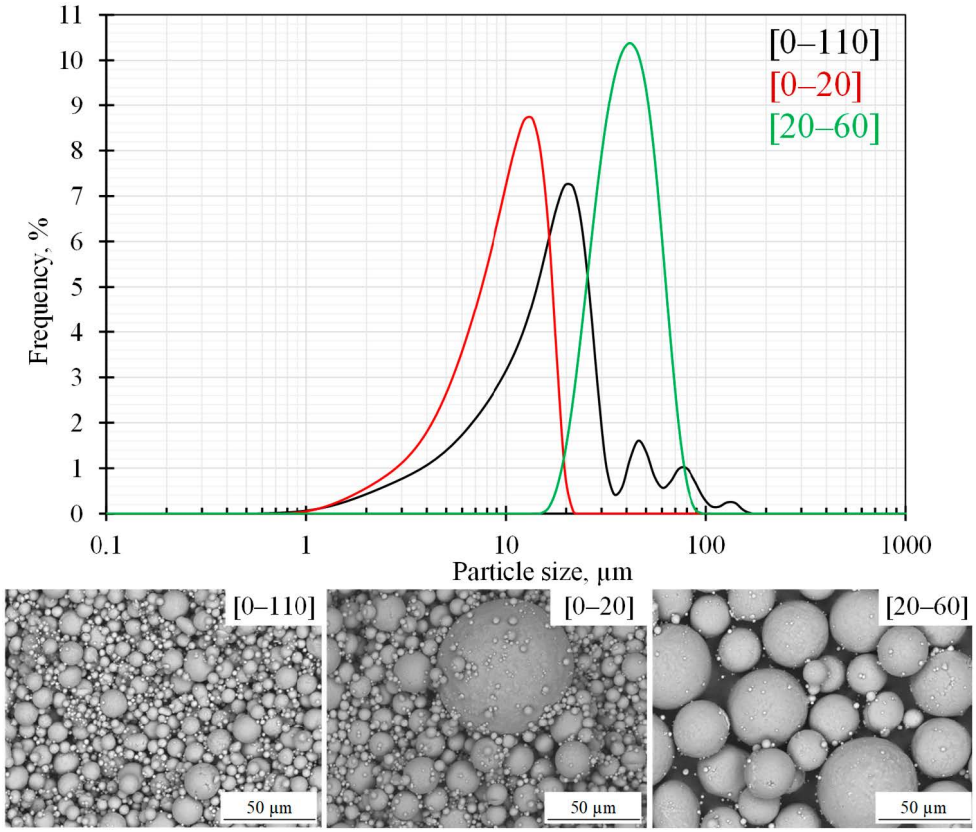

Figure 1. Powder size distributions and SEM micrographs for wide-PSD-grade [0–110], MIM-grade [0–20], and BJ-grade [20–60] powders.

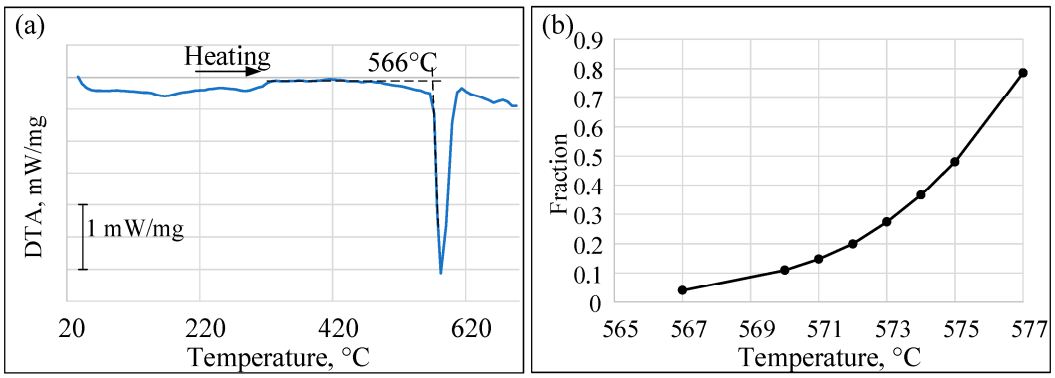

Figure 2. (**a**) DTA plot of melting behavior of atomized powder, and (**b**) liquid fraction as a function of temperature calculated using FactSage thermodynamic software.

The loose powder was inserted into stainless-steel cylindrical molds (15 mm in diameter and 10 mm in height) and slightly compacted. The cylinders were placed in a stainless-steel container along with Mg pellets (~20 g in total) in close proximity (Figure 3a). High-purity nitrogen (99.998%) purging gas was subjected to a second-stage purification process (Gettering Furnace Gas Purifier System, Centorr Model 2A-100-SS, Centorr vacuum Industries, Nashua, NH, USA) to reach 10–11 ppm of oxygen before the furnace was filled, and an inert environment was maintained. All sintering experiments were conducted in a tube furnace (Lindberg model 54579, Lindberg, Michigan, USA) under a continuous flow of nitrogen (5 L/min). The temperature during sintering was monitored using a thermocouple positioned directly above the powder samples.

Figure 3. Stainless-steel container with Mg pellets and AlSi10Mg powder before sintering (**a**) and samples after sintering (**b**,**c**): sample #4 (**b**) and sample #7 (**c**).

Samples #1–#5 were prepared using the wide-PSD-grade powder and sintered at T_s = 550, 566, 571, 575, and 579 °C, respectively. As presented in Figure 4a, the heating was performed using four (4) segments, taking approximately 5 h in all to reach the sintering temperature (T_s). The first segment was performed using a heating rate of 3 °C/min, followed by a first stabilization plateau at 350 °C for 0.5 h. During the second segment, the same heating rate of 3 °C/min was used before a second stabilization plateau at 450 °C for 0.5 h. During the third segment (between 450 °C and T_s − 10 °C), the heating rate was decreased to 1 °C/min. Then, during the fourth segment, the rate was again decreased to 0.5 °C/min up to T_s in order to minimize the temperature overshoot seen in Figure 4b. These heating cycles were followed by a sintering plateau (with a dwell time of 2 h [40]) before a cooling rate of about 5 °C/min was applied, and the samples were cooled down to under 100 °C for approximately 12 h, as shown in Figure 4a. These specific heating and cooling cycles were chosen to ensure a uniform temperature distribution within the samples, prevent distortion caused by excessive liquid formation, and minimize temperature overshoot. In fact, an overshot of about 5 °C was observed during heating (Figure 4b). Samples #8 and #9 were prepared using the MIM-grade powder and the BJ-grade powder employing the same sintering route as for sample #4 (Figure 4a,b and Table 2).

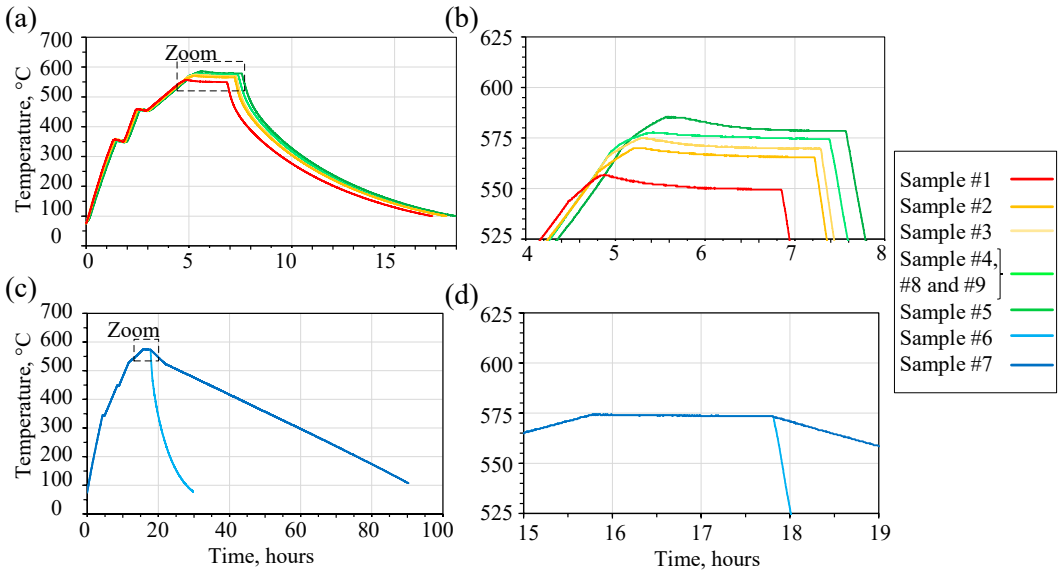

Figure 4. Temperature profiles for the sintering process: (**a**,**b**) samples #1–#5, #8, and #9, and (**c**,**d**) samples #6 and #7.

Samples #6and #7 were sintered at 575 °C for 2 h using the same wide-PSD-grade powder, but with different heating and cooling rates from the previous samples. As reported in Figure 4c, the heating was performed using four (4) segments, but this time taking 15 h, i.e., three times longer, to reach the sintering temperature. Using a similar ramp

and plateau strategy, the first two segments were performed using heating rates of 1 and 0.5 °C/min, followed by two stabilization plateaus at 350 and 450 °C for 0.5 h. The third and fourth segments were then performed at 0.5 and 0.2 °C/min up to 565 and 575 °C, respectively, in order to avoid the temperature overshoot seen in Figure 4d. These heating cycles were followed by a similar sintering plateau for 2 h before two different cooling rates were applied. On the one hand, sample #6 was cooled at 100 °C using a similar cooling rate of about 5 °C/min (taking approximately 12 h, as shown in Figure 4c and Table 2). On the other hand, sample #7 was cooled from 575 to 530 °C at 0.2 °C/min, and then up to 100 °C using a cooling rate of 0.1 °C/min (taking approximately 70 h, as shown in Figure 4c and Table 2), to further minimize the distortion of the final parts. Figure 3b,c show samples #4 and #7. Although these images represent only two samples processed under different SLPS conditions, all the others retained their cylindrical shape, indicating that particle bonding was achieved regardless of the sintering conditions.

Table 2. Summary of all sintered samples and sintering conditions.

Powder Grade	PSD	Sample Number	Heating Duration (h)	Sintering Temperature (°C)	Sintering Holding Time (h)	Cooling Duration (h)
Wide PSD grade	[0–110]	#1	5	550	2	12
		#2	5	566	2	12
		#3	5	571	2	12
		#4	5	575	2	12
		#5	5	579	2	12
		#6	15	575	2	12
		#7	15	575	2	70
MIM grade	[0–20]	#8	5	575	2	12
BJ grade	[20–60]	#9	5	575	2	12

All sintered samples were removed from the mold, cut in half, hot-mounted in conductive Bakelite, and mirror-polished (with 0.05 µm colloidal silica) before being characterized using X-ray diffraction (XRD), optical microscopy, scanning electron microscopy (SEM), and energy-dispersive X-ray spectroscopy (EDX). XRD analysis was performed on the sintered samples as well as on the raw powder (wide-PSD-grade) using an Anton Paar XRDynamic 500 diffractometer, equipped with a Cu Kα X-ray source operating at 40 kV and 40 mA. The XRD scans were conducted in the continuous scan mode over a 10–85° 2θ range, with a step size of 0.01° and a time of 100 s per step. The sintered samples were then observed with an Olympus LEXT OLS4100 laser-scanning confocal microscope and an SEM Hitachi SU8230, both in an unetched condition. EDX analysis was performed at voltages ranging between 5 and 15 kV, using a high-sensitivity FlatQuand detector (QUANTAX FlatQUAD, Bruker, Billerica, MA, USA) to detect both low- and high-energy elements, including O, N, Al, Si, and Mg. Finally, selected samples (#1, #4, and #7) were manually fractured in bending to analyze their internal features using the same SEM described above.

3. Results

3.1. XRD Diffractograms of Dry Powder and Sintered Samples

The XRD diffractograms of the raw material powder (benchmark) and sintered samples are shown in Figure 5. In addition to the prominent Al and Si peaks, several small peaks, initially absent from the raw powder, were detected in the sintered samples (indicated by vertical dashed lines in the XRD diffractogram). These nine small peaks, observed

at 2θ = 33.24, 36.07, 37.96, 49.86, 59.38, 66.10, 71.48, 72.68, and 76.52°, were identified using the ICDD database as belonging to the hexagonal AlN phase, with lattice parameters a = 3.11 Å and c = 4.98 Å. Additionally, very small peaks observed between 33 and 36° both in the powder and sintered samples were identified as the α- or β-AlFeSi phase. No peaks corresponding to Al_2O_3, AlON, $MgAl_2O_4$, MgN, Mg_3N_2, MgO, or SiO were detected for all sintered samples. This absence is likely due to the amorphous nature of these phases, their small volume fraction, and/or their complete absence. Therefore, the presence of these phases cannot be confirmed or definitively ruled out based on the XRD results.

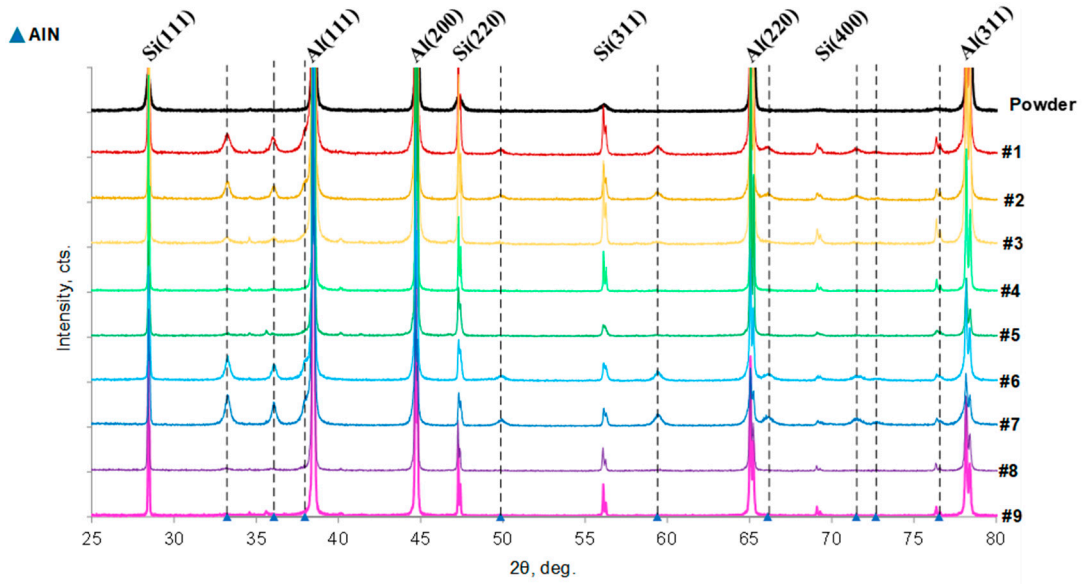

Figure 5. XRD patterns obtained for powder and sintered samples.

The broadening of the AlN peaks suggests the presence of fine-grained AlN crystal structures. The intensity of these peaks depends on the sintering conditions and the powder batches used. A Rietveld quantitative analysis [41] of the XRD diffractograms was performed to determine the volume fraction of the AlN phase. For samples produced with the wide-PSD-grade powder, the AlN volume fraction calculated in samples #1 and #2 (sintered at 550 and 566 °C) was 10.2 and 7.0%, respectively. However, this fraction significantly decreased below 2 vol.% for samples sintered between 571 and 579 °C: 1.5 vol.% for sample #3, 1.7 vol.% for sample #4, and 1.6 vol.% for sample #5. Notably, a slower heating rate up to the sintering plateau at 575 °C (sample #6), along with a reduced cooling rate (sample #7), had a pronounced effect on the AlN peak intensity observed in the XRD diffractograms (Figure 5). Samples #6 and #7 exhibited the highest AlN volume fractions at 18.5 and 29.2 vol.%, respectively. In contrast, samples #8 and #9, prepared using other powder batches (MIM-grade and BJ-grade) but sintered under the same conditions as sample #4, exhibited AlN volume fractions of 4.7% and 0.5%, respectively, confirming the influence of powder PSD on AlN formation.

3.2. Optical Micrographs of Sintered Samples

Figure 6 presents a metallographic analysis of the samples sintered at various temperatures and heating/cooling rates, using powders with different PSDs. All samples exhibit white and gray regions within the dense areas (Figure 6), corresponding to the α-Al- and Si-rich phases, respectively, as typically observed in the AlSi10Mg alloy.

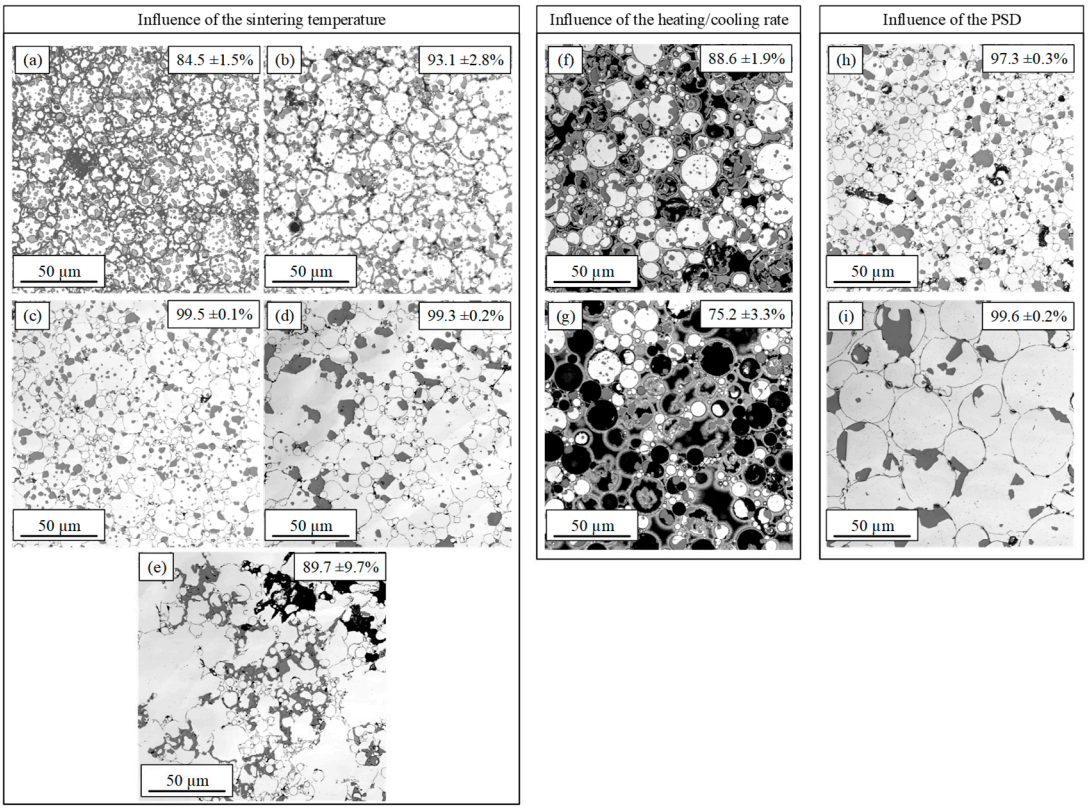

Figure 6. Optical micrographs of the sintered samples showing the influence of the sintering temperature (**a**–**e**), heating and cooling rates (**f**,**g**), and powder PSD (**h**,**i**). Samples: (**a**) #1, (**b**) #2, (**c**) #3, (**d**) #4, (**e**) #5, (**f**) #6, (**g**) #7, (**h**) #8, and (**i**) #9. The measured density values are indicated in each image.

The morphology and size of the Si phase differed noticeably between samples #1–#3 sintered at low temperatures (Figure 6a–c) and those sintered at higher temperatures (samples #4 and #5; Figure 6d,e). In particular, the Si particles in sample #4 (Figure 6d) were coarser than those in samples #1–#3 (Figure 6a–c), although the Si phase remained uniformly distributed within the α-Al matrix. In sample #5, the Si phase appeared agglomerated between powder particles, suggesting that the sintering temperature of 579 °C may have been high enough to induce the partial dissolution of Si into the Al-rich liquid phase formed during SLPS. This may have resulted in a local Si enrichment and subsequent reprecipitation near interparticle boundaries (Figure 6e).

Despite the formation of particle bonding in samples sintered within the 550–579 °C range (Figure 6a–e), varying levels of porosity were observed. The corresponding sample densities, determined via image analysis, are indicated in Figure 6a–e. At low sintering temperatures (samples #1 and #2), the occurrence of micropores was high between powder particles (Figure 6a,b). Sintering at 571 and 575 °C (samples #3 and #4, respectively) resulted in smaller micropores in the interparticle spaces, higher overall density, and a more continuous microstructure (Figure 6c,d). An increase in the sintering temperature to 579 °C (sample #5) also resulted in a continuous microstructure; however, the presence of non-uniformly distributed macropores resulted in a reduced overall density (Figure 6e). These pores in sample #5 were likely caused by excessive liquid-phase formation, its uneven distribution, particle clustering, gas entrapment, and localized overheating during sintering. All samples exhibited a distinct layer surrounding the powder particles (Figure 6a–e). Notably, the samples sintered between 571 and 579 °C showed much thinner interparticle boundaries compared with those sintered at 550 and 566 °C. In some regions, these interparticle boundaries lost their circular shape due to the formation of a liquid

phase and subsequent material reorganization. As the sintering temperature increased from 571 to 579 °C, the boundaries became increasingly indistinct, particularly around coarser powder particles, suggesting that a significantly larger volume of the liquid phase disrupted the particle surface during sintering.

The optical micrographs in Figure 6f,g illustrate the detrimental effect of a prolonged heating duration in reaching the sintering plateau. While a sintering plateau at 575 °C proved optimal for sample #4, it became evident that a slower heating rate—three times longer in this case—impeded proper densification. Indeed, sample #6 showed a discontinuous microstructure (Figure 6f) characterized by powder particles surrounded by a distinct thick gray layer. Some particles even appeared hollow, with only the gray shell-like outer layer remaining. Applying the same slow heating rate up to 575 °C, combined with an extremely slow cooling rate (over 70 h to 100 °C), further exacerbated the particle emptying phenomenon in sample #7, as shown in Figure 6g.

In contrast, samples #8 and #9, sintered using the MIM-grade and BJ-grade powders, respectively, exhibited continuous microstructures and particle contours similar to those obtained in sample #4, i.e., produced using the same sintering profile (Figure 6h,i vs. Figure 6d). The finer powder used in sample #8 (Figure 6h) led to higher porosity compared with the coarser powder used in sample #9 (Figure 6i). Tandon [39] suggests that such differences may stem from the varying amount of the liquid phase generated during the SLPS process for powders with different particle sizes, a factor influenced by the solidification conditions during atomization. Additionally, particle rearrangement during SLPS may differ between PSDs due to differences in particle packing, as well as variations in the oxygen content within the powder bed.

3.3. Characterization of Powder Particle Bonding

3.3.1. Effect of Sintering Temperature and Powder PSDs

Figure 7 shows typical high-magnification SEM micrographs of samples sintered between 550 and 579 °C using different PSDs. Samples #1 and #2 exhibited either no metallurgical bonding or only limited interparticle connections. As shown in Figure 7a, the SEM image clearly reveals that the powder particles remained largely isolated, surrounded by a surface layer formed during sintering. This layer likely inhibited effective bonding and material reorganization. In sample #1, the layer had an average thickness of approximately 350 nm, while in sample #2, the thickness varied significantly, reaching up to 700 nm in certain regions. Moreover, Figure 7b,d reveal dendritic growth within these layers, with dendrites oriented perpendicular to the powder surface.

In contrast, samples #3 to #5 exhibited well-developed metallurgical bonding between powder particles, characterized by the visible filling of the interparticle spaces and minimal voids (Figure 7e,g,i). At a higher magnification (Figure 7f,h,j), a thin layer was also observed growing perpendicularly from the particle surfaces, likely with a dendritic structure, particularly evident in sample #3 (Figure 7f). For these samples, the layer thickness ranged between 100 and 200 nm, with an average of around 150 nm, regardless of the sintering temperature varying from 571 to 579 °C.

A similar layer morphology was observed in samples #8 and #9, which were prepared using MIM-grade and BJ-grade powders, respectively, and sintered at 575 °C for 2 h (Figure 7k–n). The layer in sample #9 exhibited a thickness comparable to that in samples #3 to #5 (100–200 nm), whereas sample #8 showed a thinner layer, closer to 100 nm.

Figure 8 presents EDX line scans across samples #1 and #4 (sintered at 550 and 575 °C, respectively). The scan covered two metal particles, the liquid-filled region between them, and the interfacial layer. The α-Al matrix was primarily composed of aluminum, while the

interfacial layer showed a reduced Al concentration, suggesting the formation of secondary phases (Figure 8a). In sample #4, a well-defined Al-enriched filled region was observed (Figure 8b), with an aluminum concentration comparable to that of the α-Al matrix. This indicates enhanced particle coalescence, likely driven by the SLPS process.

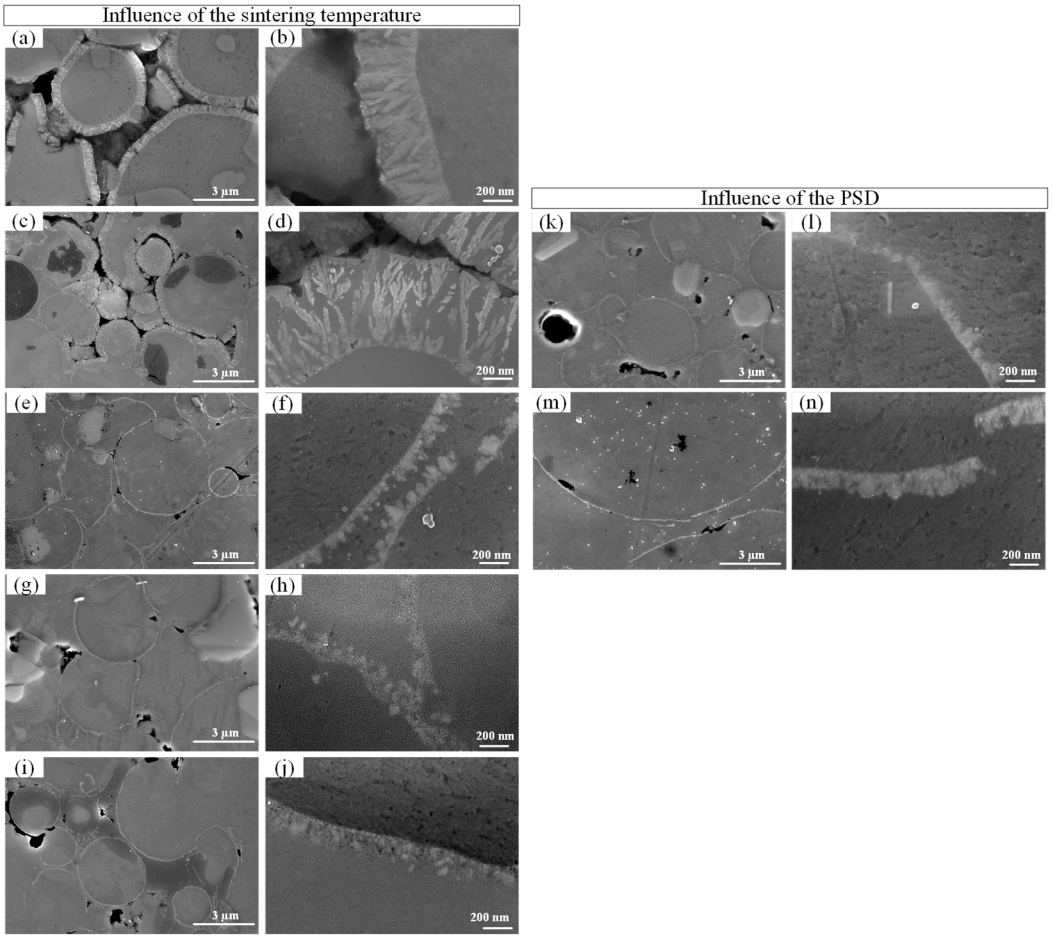

Figure 7. SEM images of samples: (**a**,**b**) #1, (**c**,**d**) #2, (**e**,**f**) #3, (**g**,**h**) #4, (**i**,**j**) #5, (**k**,**l**) #8, and (**m**,**n**) #9.

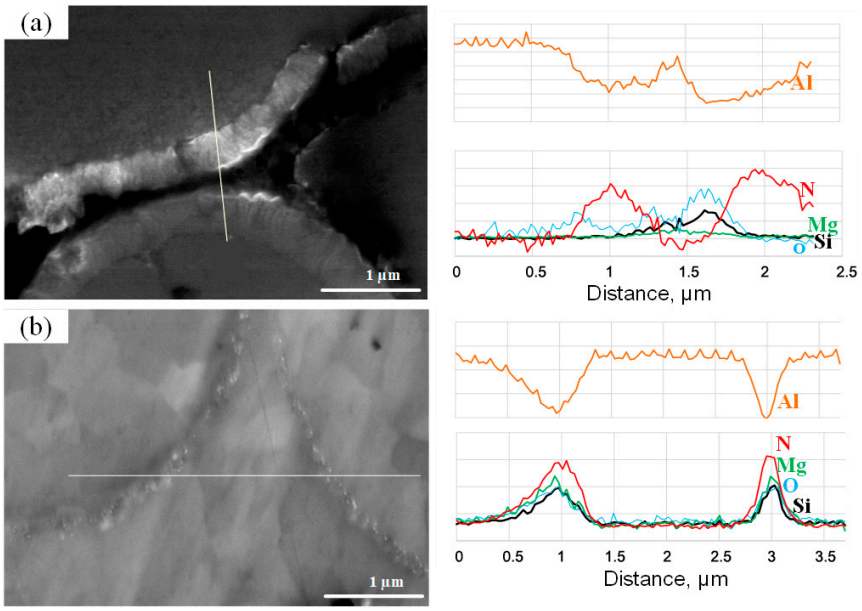

Figure 8. SEM-EDX line analysis of interparticle boundaries for samples #1 (**a**) and #4 (**b**). White lines in the SEM images indicate the locations of the EDX line analysis.

EDX analysis confirmed the presence of N in the interfacial layer surrounding powder particles in both samples, consistent with the formation of an AlN layer. In sample #4 (Figure 8b), O and Mg were also detected within the layer. The localization of Mg and O intensity peaks near the particle/layer interface suggests that Mg may have reduced the surface Al_2O_3, thereby enabling nitridation. Additionally, sample #1 exhibited Si and O peaks in the region between the powder particles (Figure 8a), while in sample #4, the peaks of N and Si were shifted toward the outer part of the interfacial layer, coinciding with a minimum in the Al concentration (Figure 8b). This suggests a possible role of Si in the nitriding mechanism, although its precise contribution remains unclear. Notably, prior studies on AlSi10Mg alloys [42] have reported a correlation between an increased Si content and a higher N concentration within the AlN layer. As proposed by Li et al. [43], Si may enhance nitridation by promoting N diffusion through the formation of Si_3N_4.

Given the apparent heterogeneity of the nitride layer, it is possible that it consisted of a composite AlN/Al structure containing aluminum-filled channels. These channels could have facilitated Al migration toward the surface, enabling continued nitridation driven by a chemical potential gradient.

Moreover, the presence of a clearly defined AlN/Al layer and a liquid-filled region between particles in sample #4 suggests that nitriding began before the onset of SLPS. Once SLPS started at 575 °C, further AlN/Al layer formation appeared to be suppressed. Consequently, the AlN/Al layer in sample #4 was thinner than in sample #1, where SLPS did not occur or was significantly less active at 550 °C, i.e., a temperature too low to generate a protective liquid phase around particle boundaries, leaving them exposed to the nitrogen atmosphere.

3.3.2. Effect of Heating and Cooling Rates

Figure 9 shows SEM micrographs of samples #6 and #7, both sintered at 575 °C using a slow heating rate, with sample #6 cooled under standard conditions and sample #7 cooled using a slow rate. Both samples exhibited a distinct surface layer characterized by columnar features. Similar to sample #1 (Figure 8a,b), sample #6 showed dendritic growth within the layer (Figure 9c), with dendrites oriented perpendicularly to the powder surface. The absence of globular Si in the thicker regions of the layer, along with noticeable variation in layer thickness, supports an outward growth mechanism (Figure 9a,b). In regions where particles were closely spaced, the layer thickness was approximately 150 nm, similar to that observed in samples #3–#5 (Figure 9b), with some evidence of coalescence. In contrast, isolated particles (not in close contact) developed a significantly thicker layer (up to ~1 µm; Figure 9b). Additionally, the reduced interparticle gaps indicate a degree of self-densification within the sample.

Sample #7 exhibited similar microstructural features (Figure 9d–g) but also showed evidence of bidirectional AlN growth, both outward and inward into the particle interior, based on the distribution of the Si phase, which was present in the inward-growing region and absent in the outward-growing region (Figure 9d). The interface between these two growth directions was particularly evident near round pores, as indicated by the yellow arrows in Figure 9d. This bidirectional growth led to a thicker AlN layer, reaching up to ~3 µm. These internal pores were located within the original powder particles and were surrounded by the AlN/Al layer, which covered both the internal surfaces and the Si phase. As proposed by Vispute et al. [44], this phenomenon may result from epitaxial AlN/Al growth on Si(111), driven by basal plane alignment between AlN and Si.

The mechanism behind the inward growth of the AlN/Al layer remains less well-understood, likely due to the low nitrogen diffusion coefficient in AlN [22]. However, similar inward growth behaviors have been reported in previous studies [15,45,46]. As

noted in [42], cracking of the AlN/Al shell may occur when its thickness exceeds 2 µm, due to stresses induced by the coefficient of thermal expansion (CTE) mismatch between Al and AlN/Al [45]. Once cracking occurs, liquid aluminum may escape through these cracks, filling voids between powder particles by capillarity action and forming rounded pores (Figure 9g). Furthermore, if the AlN/Al shell impeded particle consolidation, the liquid aluminum may remain trapped in interparticle regions, where it can react with nitrogen in the surrounding atmosphere, resulting in additional AlN/Al formation between particles.

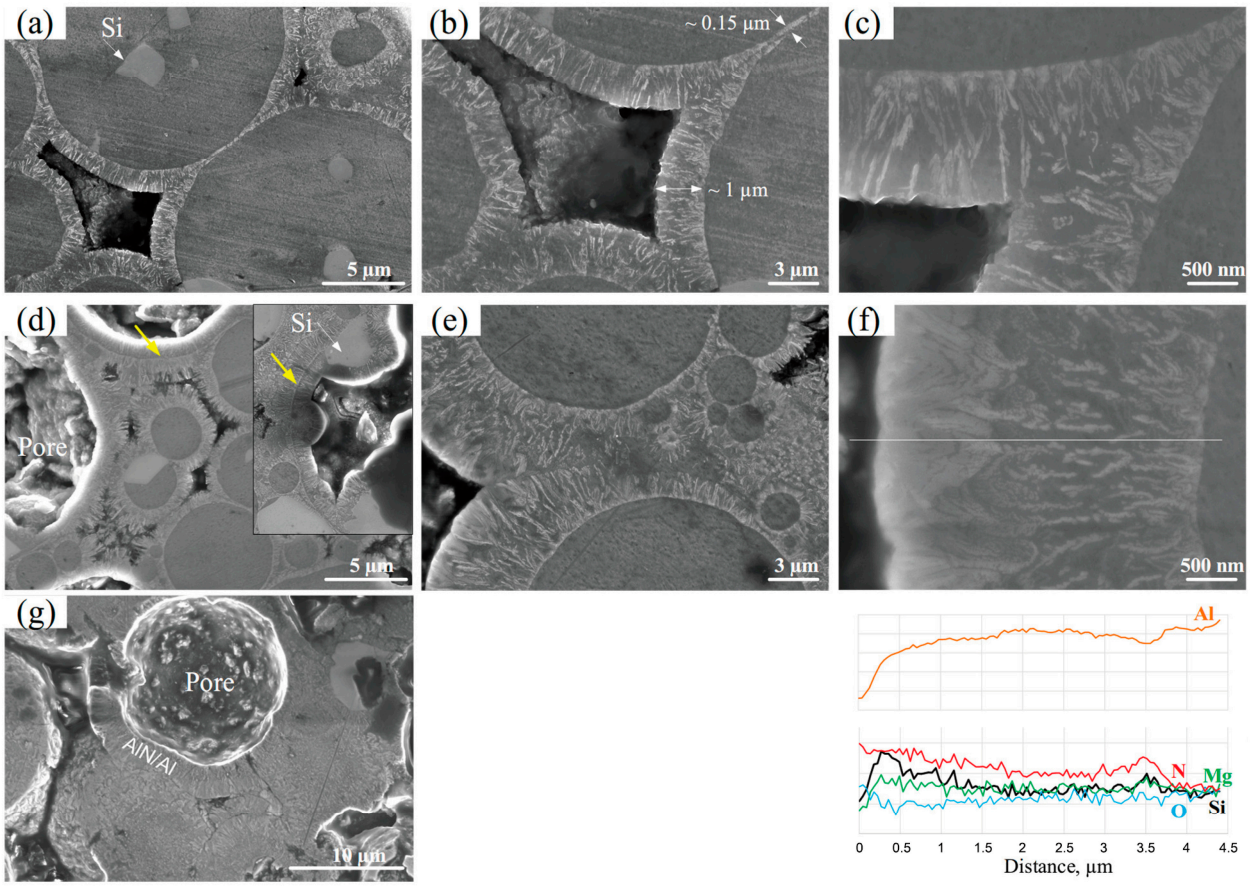

Figure 9. SEM images of samples: (**a**–**c**) #6 and (**d**–**g**) #7. EDX line analysis of surface layer in sample #7 is inset in (**f**), white lines in (**f**) indicate the locations of the EDX line analysis.

Additionally, both samples exhibited microstructural variations across the thickness of the AlN/Al layer (Figure 9c), suggesting changes in growth conditions during sintering. A high density of fine AlN dendrites near the particle/layer interface indicated rapid nucleation and diffusion-driven growth. Continued dendrite development was likely sustained by the capillary transport of Al between the growing dendrites [47–49], driven by a chemical potential gradient. The good wettability of Al on AlN facilitated the infiltration of liquid aluminum into the evolving composite layer. In sample #7, the slow cooling rate promoted the formation of a coarser and denser AlN/Al structure in the outer layer (Figure 9f), consistent with the observations reported by Rogers et al. [15]. This coarser region also displayed increased concentrations of N and Si, while Mg and O levels remained relatively constant throughout the layer (Figure 9f).

3.4. Morphology of AlN Layer

To investigate the surface morphology of the nitrided layer, samples #1, #4, and #7 were fractured by bending, and their fracture surfaces are shown in Figure 10. The fracture surface of sample #1 (Figure 10a,b) exhibited features typical of brittle rupture, indicative of

poor interparticle bonding. This behavior is consistent with the absence of the SLPS process expected at this low sintering temperature (550 °C) and high heating rate. The AlN/Al layer was clearly visible on the surface of the powder particle (Figure 10c). In some regions, the growth of this layer appeared to be inhibited, likely due to the presence of secondary phases, such as AlFeSi and Si. The surface cracks marked by white arrows in Figure 10c could be attributed either to the fracture process itself or to the mismatch in CTEs between the α-Al matrix and the nitrided layer.

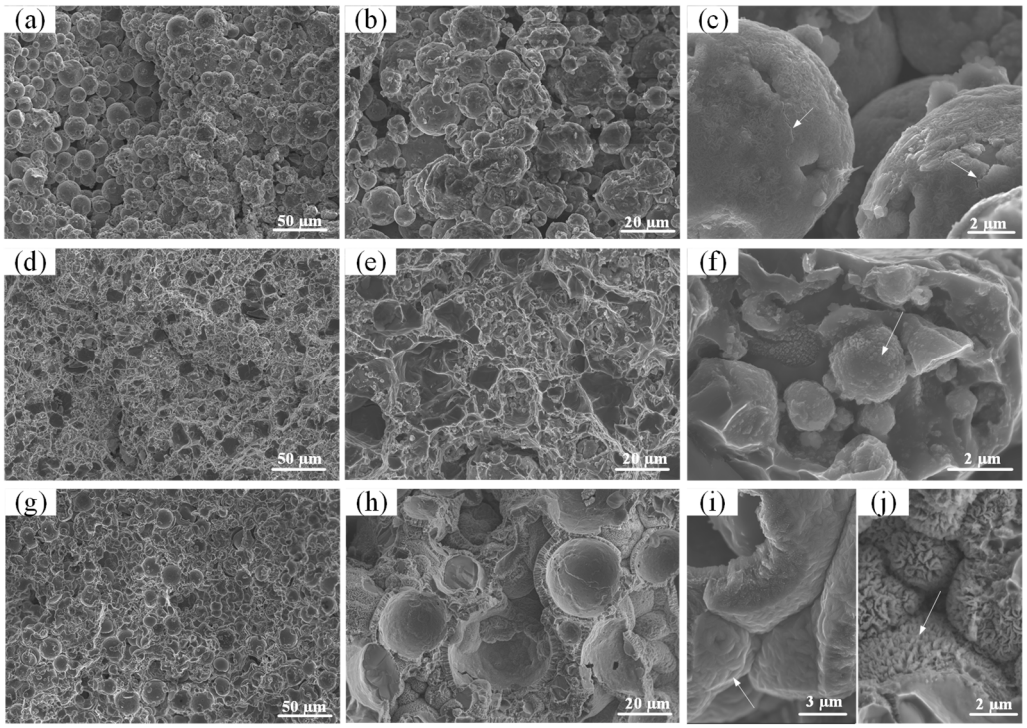

Figure 10. Fracture surfaces of samples #1 (**a**–**c**), #4 (**d**–**f**), and #7 (**g**–**j**).

In contrast, the fracture surface of sample #4 (Figure 10d,e) primarily exhibited features related to ductile rupture, as evidenced by the presence of dimples, confirming effective densification and strong metallic bonding between particles. This is consistent with the optimal sintering condition of 575 °C and a high heating rate. Notably, some dimples contained fine AlN particles at their centers, as indicated by the white arrow in Figure 10f.

The fracture morphology of sample #7 (Figure 10g,h) was, again, predominantly brittle, similar to that of sample #1, despite being sintered at an elevated temperature (575 °C, but using a low heating rate), where SLPS would typically be expected. Higher magnification confirmed that the nitrided layer formed a thick shell around the powder particles (Figure 10h–j). Unlike in sample #1, however, the fracture in sample #7 occurred along the shell itself, particularly in regions where the aluminum was either fully consumed or had escaped, leaving the particles devoid of α-Al. The shell surface appeared rough, with features often oriented perpendicularly to the original powder surface (Figure 10h,i).

Two distinct surface morphologies of the shell were observed in sample #7: (1) dense, coarse feather-shaped nitrides (indicated by a white arrow in Figure 10i), and (2) fine dendritic nitrides (indicated by a white arrow in Figure 10j). The feather-shaped nitrides likely correspond to the outer AlN layer previously observed in SEM images (Figure 10f). These structures are believed to form during extended sintering, resulting from prolonged exposure to nitrogen at elevated temperatures. This morphology is consistent with previous studies on AlN structures [50]. Conversely, the fine dendritic shell, characterized by elongated, sharp features (Figure 10j), results from the rapid nucleation and growth of

the nitride layer during the initial stage of nitriding (during heating and/or isothermal holding). These fine dendrites tended to form on particles that were in close proximity, where the spatial constraint likely inhibited the growth of coarser feather-shaped nitrides.

4. Discussion

The use of a nitrogen atmosphere and the addition of magnesium powder are central to the successful sintering of aluminum alloys. These measures are known to disrupt the native aluminum oxide layer, which otherwise inhibits particle bonding and adversely affects the wetting behavior during the SLPS process. This strategy has proven effective for various aluminum alloys, including conventional hypereutectic aluminum cast alloys (>12 wt.% Si) [51–54]. However, in the case of the AlSi10Mg alloy—containing approximately 10 wt.% Si and 0.35 wt.% Mg—careful optimization of sintering parameters is essential. These parameters include the heating and cooling rates, sintering temperature, and duration of nitrogen exposure, due to the alloy's heightened susceptibility to nitriding.

In this study, the role of pure magnesium, placed in the vicinity of AlSi10Mg samples in the furnace, could not be conclusively verified. As reported in [14], magnesium vaporizes at temperatures above 550 °C. This vapor, carried by the nitrogen flow, may reduce Al_2O_3 and, thus, facilitate nitriding [1,19]. However, the formation of a nitrided layer in the sample sintered at 550 °C suggests that the magnesium powder likely played only a limited role, primarily acting as an oxygen scavenger rather than an active reduction agent for aluminum oxide.

Magnesium already present in the alloy can diffuse to the particle surfaces, a process that accelerates above 400 °C [55,56]. Once at the surface, Mg disrupts the oxide layer and promotes the formation of AlN. As reported in [42], the AlN growth rate increases with the Mg content, following a parabolic trend governed by diffusion. In the AlSi10Mg alloy, nitriding has been observed around 460 °C [42], which is below the onset of the SLPS process at 566 °C. Therefore, if nitriding occurs before or within this temperature range, the thickness of the AlN layer formed during heating becomes a key factor in controlling the sintering process.

The results showed that exposing AlSi10Mg powder to nitrogen for 4.0 to 4.5 h at temperatures between 460 and 566 °C resulted in the formation of an AlN/Al layer with a thickness ranging from 350 to 700 nm (Figure 11). In contrast, samples exposed for a similar duration (4.7 h ± 0.1 h) but at temperatures between 460 and 579 °C formed a significantly thinner AlN layer (~150 nm). This decrease in AlN thickness is attributed to the occurrence of the SLPS process at temperatures above 566 °C. During SLP, powder reorganization and mass transport rapidly reduce pore interconnectivity, eventually cutting off the nitrogen supply required for the nitriding reaction.

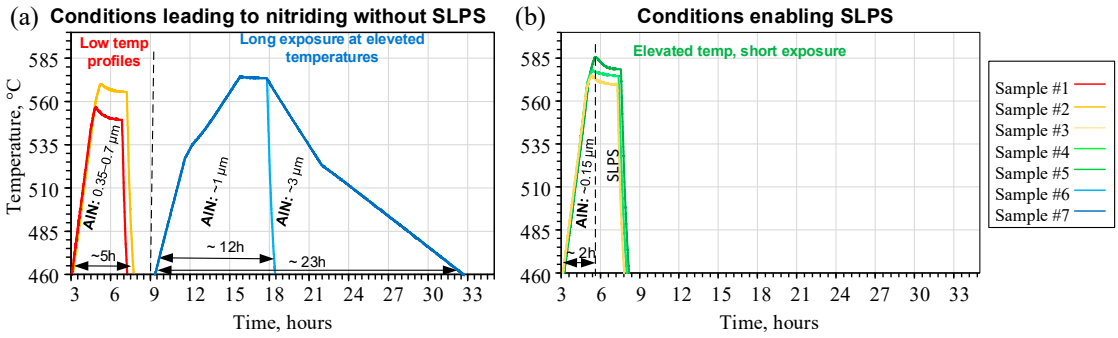

Figure 11. Sintering conditions on AlN formation (**a**) and SLPS (**b**).

Although the AlN layer thickness remained relatively constant (~150 nm) under optimized sintering conditions (575 °C), the volume fraction of AlN varied with the PSD.

For fine powders (0–20 μm), the AlN content reached nearly 5 vol. %, compared with 0.5–2 vol.% in samples exhibiting broader PSDs (0–110 and 20–60 μm). Previous work [57] has demonstrated that smaller particles lead to higher reaction rates and increased AlN formation over time. However, this trend could not be conclusively confirmed in the present study as the AlN layer thickness was approximately the same across different particle size ranges. The higher AlN volume fraction detected by XRD in finer powders is, therefore, attributed to their increased specific surface area.

Extended exposure to nitrogen, achieved through a slow heating rate up to 575 °C (without initiating SLPS), resulted in significant thickening of the AlN layer. For example, a 12 h exposure in the 460–575 °C range led to the formation of a ~1 μm thick layer (Figure 11a), with the AlN phase content rising to 18.5 vol.%. In comparison, a shorter 4.8 h exposure in the same temperature range produced only ~2 vol.% of AlN (Figure 11b). When both slow heating and slow cooling were applied—resulting in a total exposure time of 23 h—the layer thickness increased further to ~3 μm, and the AlN content approached 30 vol. % (Figure 11a). This extensive nitriding contributed to some material strengthening but did not result in significant shrinkage. The observed bonding is attributed to AlN/Al/AlN interlocking rather than true metallic sintering. The consumption of Al during nitriding causes considerable mass transport, but, due to the presence of a thick nitrided layer, which impedes the material reorganization typically occurring during SLPS, no macroscopic densification or shrinkage can take place.

These findings indicate that prolonged nitrogen exposure within the 460–575–460 °C range, in the absence of SLPS activation, promotes extensive AlN formation, which can hinder densification and degrade mechanical properties. Optimizing the heating duration to less than 2 h before reaching the sintering plateau ($571 \leq T_s \leq 579$ °C) effectively limits AlN growth. Under these conditions, the nitrided layer remains sufficiently thin to be penetrated by the liquid phase, enabling material reorganization, transport, and densification.

Nevertheless, the influence of the AlN phase on the final material properties requires further investigation. If AlN is found to be detrimental, its content can be reduced by selecting coarser and narrower PSD powders in order to minimize the total surface area and limit AlN formation. Moreover, alternative approaches, such as sintering under a partial pressure of N_2 or switching from N_2 to an inert atmosphere, should be explored to limit the AlN formation while preserving its beneficial effect during the sintering of the AlSi10Mg alloy.

5. Conclusions

This study investigated the influence of supersolidus liquid-phase sintering (SLPS) conditions on AlN phase formation and particle bonding in AlSi10Mg under a nitrogen atmosphere. The sintering temperatures ranged from 550 to 579 °C, with a holding duration of 2 h, two heating durations, 5 and 15 h, and two cooling durations, 12 and 70 h. Three AlSi10Mg powders having different particle size distributions (0–110, 0–20, and 20–60 μm) were used. The key findings are summarized as follows:

(1) AlN-phase formation was observed in all samples regardless of the specific sintering parameters. The AlN layer formed on the surface of AlSi10Mg particles, growing outward in a columnar pattern.

(2) Sintering at temperatures between 571 and 579 °C led to improved densification, minimized AlN formation, and enhanced particle bonding. Nevertheless, even under similar SLPS conditions, the AlN fraction varied with the powder PSDs: a finer powder resulted in a higher AlN content due to its greater surface area.

(3) Low sintering temperatures (below 566 °C) or slow heating rates (0.2–0.5 °C/min) promoted the formation of a thick AlN shell around metal particles. Under slow heating rates, the AlN content reached up to ~30 vol.%. However, true metallic bonding was not achieved; instead, the structure was held together by an AlN/Al/AlN interlocking network. The overall sample density remained low, partly due to the formation of hollow particles, caused by the complete consumption of aluminum through the nitriding reaction.

Author Contributions: Conceptualization, A.K., R.P., and V.D.; methodology, M.K.T. and A.C.; validation, A.K., M.K.T., R.P., and V.D.; investigation, M.K.T.; writing—original draft, A.K.; writing—review and editing, R.P. and V.D.; visualization, A.K.; supervision, A.K. and V.D.; project administration, V.D.; funding acquisition, V.D. All authors have read and agreed to the published version of this manuscript.

Funding: This project was funded by the National Research Council of Canada (the National Program Office; proposal #AM-125-1) and the Centre Québécois de Recherche et de Développement de l'Aluminium (project #1148).

Data Availability Statement: The datasets generated during the current study are available from the corresponding author upon a reasonable request.

Acknowledgments: The authors would like to thank the NRC R&D industrial group METALTec for initiating this project, with special thanks to the industrial partners AP&C and Dana Incorporated for their active participation in this project.

Conflicts of Interest: The authors declare no conflicts of interest.

References

1. Schaffer, G.B.; Hall, B.J. The influence of the atmosphere on the sintering of aluminum. *Metall. Mater. Trans. A* **2002**, *33*, 3279–3284. [CrossRef]
2. Pieczonka, T. Disruption of an Alumina Layer During Sintering of Aluminium in Nitrogen. *Arch. Metall. Mater.* **2017**, *62*, 987–992. [CrossRef]
3. Trunov, M.A.; Schoenitz, M.; Dreizin, E. Effect of polymorphic phase transformations in alumina layer on ignition of aluminum particles. *Combust. Theory Model.* **2006**, *10*, 603–623. [CrossRef]
4. Pieczonka, T.; Kazior, J. Microstructure Evolution during Sintering of Aluminium in Nitrogen. *Adv. Mater. Res.* **2013**, *811*, 64–71. [CrossRef]
5. Boyes, W. (Ed.) *Instrumentation Reference Book*, 4th ed.; Butterworth-Heinemann: Boston, MA, USA, 2010.
6. Schaffer, G.B.; Sercombe, T.B.; Lumley, R.N. Liquid phase sintering of aluminium alloys. *Mater. Chem. Phys.* **2001**, *67*, 85–91. [CrossRef]
7. Oya, N.; Sato, T.; Yamaguchi, D. In Situ scanning electron microscopy observation of sintering process of aluminum alloy. *Mater. Trans.* **2023**, *64*, 1946–1951. [CrossRef]
8. German, R. Phase diagrams in liquid phase sintering treatments. *JOM* **1986**, *38*, 26–29. [CrossRef]
9. German, R.M.; Suri, P.; Park, S.J. Review: Liquid phase sintering. *J. Mater. Sci.* **2009**, *44*, 1–39. [CrossRef]
10. Kehl, W.; Fischmeister, H.F. Liquid Phase Sintering of Al—Cu Compacts. *Powder Metall.* **1980**, *23*, 113–119. [CrossRef]
11. Du, X.; Liu, R.; Xiong, X.; Liu, H. Effects of sintering time on the microstructure and properties of an Al-Cu-Mg alloy. *J. Mater. Res. Technol.* **2020**, *9*, 9657–9666. [CrossRef]
12. Momeni, H.; Razavi, H.; Shabestari, S. Effect of supersolidus liquid phase sintering on the microstructure and densification of the Al-Cu-Mg prealloyed powder. *Iran. J. Mater. Sci. Eng.* **2011**, *8*, 10–17.
13. Sercombe, T.B.; Schaffer, G.B. On the role of magnesium and nitrogen in the infiltration of aluminium by aluminium for rapid prototyping applications. *Acta Mater.* **2004**, *52*, 3019–3025. [CrossRef]
14. Soni, R.; Sarin, V.K.; Rao, P.; Srinivasan, E.; Basu, S.N. Growth of AlN coating on Al-6061 alloy surface. *Surf. Coat. Technol.* **2024**, *476*, 130254. [CrossRef]
15. Rogers, S.; Dargusch, M.; Kent, D. Impacts of temperature and time on direct nitridation of aluminium powders for preparation of AlN reinforcement. *Materials* **2023**, *16*, 1583. [CrossRef] [PubMed]

16. Kondoh, K.; Kimura, A.; Takeda, Y.; Watanabe, R. Behavior of magnesium and tin at the surface of aluminum-silicon-magnesium-tin alloy powder particles at elevated temperature and their effect on direct nitriding reaction. *J. Jpn. Inst. Met. Mater.* **2000**, *64*, 1106–1112. [CrossRef]
17. MacAskill, I.; Hexemer, R., Jr.; Donaldson, I.; Bishop, D. Effects of magnesium, tin and nitrogen on the sintering response of aluminum powder. *J. Mater. Process. Technol.* **2010**, *210*, 2252–2260. [CrossRef]
18. Sercombe, T.B.; Schaffer, G.B. On the role of tin in the nitridation of aluminium powder. *Scr. Mater.* **2006**, *55*, 323–326. [CrossRef]
19. Scholz, H.; Greil, P. Nitridation reactions of molten Al-(Mg, Si) alloys. *J. Mater. Sci.* **1991**, *26*, 669–677. [CrossRef]
20. Kondoh, K.; Kimura, A.; Watanabe, R. Effect of Mg on sintering phenomenon of aluminium alloy powder particle. *Powder Metall.* **2001**, *44*, 161–164. [CrossRef]
21. Kondoh, K.; Kimura, A.; Watanabe, R. Analysis of tin behaviour on surface of rapidly solidified aluminium alloy powder particles during heating. *Powder Metall.* **2001**, *44*, 253–258. [CrossRef]
22. Okada, T.; Toriyama, M.; Kanzaki, S. Direct nitridation of aluminum compacts at low temperature. *J. Mater. Sci.* **2000**, *35*, 3105–3111. [CrossRef]
23. Huo, S.H.; Qian, M.; Schaffer, G.B.; Crossin, E. 21—Aluminium powder metallurgy. In *Fundamentals of Aluminium Metallurgy*; Lumley, R., Ed.; Woodhead Publishing: Cambridge, UK, 2011; pp. 655–701.
24. Schaffer, G.B.; Yao, J.Y.; Bonner, S.J.; Crossin, E.; Pas, S.J.; Hill, A.J. The effect of tin and nitrogen on liquid phase sintering of Al–Cu–Mg–Si alloys. *Acta Mater.* **2008**, *56*, 2615–2624. [CrossRef]
25. Yan, M.; Yu, P.; Schaffer, G.B.; Qian, M. Secondary phases and interfaces in a nitrogen-atmosphere sintered Al alloy: Transmission electron microscopy evidence for the formation of AlN during liquid phase sintering. *Acta Mater.* **2010**, *58*, 5667–5674. [CrossRef]
26. Sweet, G.A.; Hexemer, R.L.; Donaldson, I.W.; Taylor, A.; Bishop, D.P. Powder metallurgical processing of a 2xxx series aluminum powder metallurgy metal alloy reinforced with AlN particulate additions. *Mater. Sci. Eng. A* **2019**, *755*, 10–17. [CrossRef]
27. Dai, D.; Gu, D.; Xia, M.; Ma, C.; Chen, H.; Zhao, T.; Hong, C.; Gasser, A.; Poprawe, R. Melt spreading behavior, microstructure evolution and wear resistance of selective laser melting additive manufactured AlN/AlSi10Mg nanocomposite. *Surf. Coat. Technol.* **2018**, *349*, 279–288. [CrossRef]
28. Comhaire, J.; Donaldson, I.W.; Bishop, D.P. Fabrication of AlSi10Mg–AlN metal matrix composites using laser powder bed fusion technology. *Can. Metall. Q.* **2024**, *64*, 362–382. [CrossRef]
29. Antolin, S.; Nagelberg, A.; Creber, D. Formation of Al_2O_3/metal composites by the directed oxidation of molten aluminum-magnesium-silicon alloys: Part I, microstructural development. *J. Am. Ceram. Soc.* **2005**, *75*, 447–454. [CrossRef]
30. Yan, Q.; Song, B.; Shi, Y. Comparative study of performance comparison of AlSi10Mg alloy prepared by selective laser melting and casting. *J. Mater. Sci. Technol.* **2020**, *41*, 199–208. [CrossRef]
31. Sathishkumar, A.; Soundararajan, R.; Sivasankaran, S. Effect of Direct Aging on the Microstructure and Mechanical Behavior of AlSi10Mg Alloy: Casting Versus Selective Laser Melting. *J. Mater. Eng. Perform.* **2023**, *32*, 3215–3229. [CrossRef]
32. Im, S.; Ghasri-Khouzani, M.; Muhammad, W.; Batmaz, R.; Esmati, K.; Chakraborty, A.; Natarajan, A.; Martin, É. Evaluation of Different Sintering Agents for Binder Jetting of Aluminum Alloy. *J. Mater. Eng. Perform.* **2023**, *32*, 9550–9560. [CrossRef]
33. KManchili, S.; Singh, G.; Missiaen, J.-M.; Bouvard, D. Additive manufacturing of aluminum Al 6061 alloy using metal injection molding granules: Green density, surface roughness, and tomography study. *Prog. Addit. Manuf.* **2025**, *10*, 2893–2909. [CrossRef]
34. Chen, B.; Moon, S.K.; Yao, X.; Bi, G.; Shen, J.; Umeda, J.; Kondoh, K. Comparison study on additive manufacturing (AM) and powder metallurgy (PM) AlSi10Mg alloys. *JOM* **2018**, *70*, 644–649. [CrossRef]
35. Kumar Ramavajjala, A.; Dandekar, T.R.; Khatirkar, R.K.; Joshi, C.; Chouhan, R.N.; Agnihotri, A. A review on the correlation between microstructure, heat treatment and mechanical properties of additively manufactured AlSi10Mg by LPBF. *Crit. Rev. Solid State Mater. Sci.* **2025**, *50*, 239–274. [CrossRef]
36. Lupi, G.; de la Vega, F.M.; de Menezes, J.T.O.; Zanon, M.; Pelletiers, T.; Castrodeza, E.M.; Casati, R. Investigation of the thermal cycle and mechanical properties of Al 6061 produced by binder jetting. *Mater. Sci. Eng. A* **2025**, *929*, 148129. [CrossRef]
37. Katsuyoshi Kondoh, A.K.a.R.W. Mechanism of In-situ Formation of AlN in Direct Nitriding Process and Characteristic of Sintered Al-AlN Composite. *Trans. Jpn. Weld. Soc.* **2001**, *19*, 383–389. [CrossRef]
38. *DIN EN 1706:2020*; Aluminium and Aluminium Alloys—Castings—Chemical Composition and Mechanical Properties. Deutsches Institut für Normung e.V. (DIN): Berlin, Germany, 2020.
39. Tandon, R. Densification Mechanisms and Microstructural Evolution Leading to High Density Processing of Prealloyed Powders in Supersolidus Liquid Phase Sintering. Ph.D. Thesis, The Pennsylvania State University, University Park, PA, USA, 1995.
40. Qian, M.; Schaffer, G.B. 12—Sintering of aluminium and its alloys. In *Sintering of Advanced Materials*; Fang, Z.Z., Ed.; Woodhead Publishing: Cambridge, UK, 2010; pp. 291–323.
41. Bish, D.L.; Howard, S. Quantitative phase analysis using the Rietveld method. *Appl. Crystallogr.* **1988**, *21*, 86–91. [CrossRef]
42. Spies, H.-J.; Dalke, A. Nitriding of Aluminum and its Alloys. In *Heat Treating of Nonferrous Alloys*; ASM International: Almere, The Netherlands, 2016; pp. 302–307.

43. Li, X.; Xin, W.; Ren, Z.a.; Wang, Y.; Wang, W. Aluminium nitride layers prepared by nitrogen arc discharge on Al-Si alloy substrate. *J. Mater. Process. Technol.* **2021**, *288*, 116847. [CrossRef]
44. Vispute, R.D.; Narayan, J.; Wu, H.; Jagannadham, K. Epitaxial growth of AlN thin films on silicon (111) substrates by pulsed laser deposition. *J. Appl. Phys.* **1995**, *77*, 4724–4728. [CrossRef]
45. Lee, K.-B.; Kim, S.-H.; Kim, D.-Y.; Cha, P.-R.; Kim, H.-S.; Choi, H.-J.; Ahn, J.-P. Aluminum matrix composites manufactured using nitridation-induced self-forming process. *Sci. Rep.* **2019**, *9*, 20389. [CrossRef]
46. Kent, D.; Drennan, J.; Schaffer, G.B. A morphological study of nitride formed on Al at low temperature in the presence of Mg. *Acta Mater.* **2011**, *59*, 2469–2480. [CrossRef]
47. Lee, K.-B.; Kim, Y.H.; Choi, H.J.; Ahn, J.-P. Effect of carbon on the nitridation behavior of aluminum powder. *J. Alloys Compd.* **2016**, *689*, 218–224. [CrossRef]
48. Lee, K.-B.; Yoo, S.-H.; Kim, H.-S.; Won, S.-O.; Yang, B.-J.; Ahn, J.-P.; Choi, H.-J. Nitridation-assisted Al infiltration for fabricating Al composites. *J. Mater. Sci.* **2017**, *52*, 4333–4344. [CrossRef]
49. Kim, S.-H.; Noh, J.-H.; Ahn, J.-P.; Lee, J.-C.; Kwon, H.; Lee, J.; Yang, H.R.; Lee, K.-B. Effects of Surface Oxide on the Nitridation Behavior of Aluminum Particles. *Metall. Mater. Trans. A* **2015**, *46*, 496–504. [CrossRef]
50. Moghadam Arya, S.; Griffiths, W. Aluminum Nitride in Al–Si–Mg Alloy. *Metall. Mater. Trans. B* **2023**, *54*, 1965–1984. [CrossRef]
51. Reinhold, B. *Untersuchungen zum Einfluss des Sauerstoffpartialdrucks beim Plasmanitrieren von Aluminiumlegierungen und Chrom-legierten Stählen*; Shaker: Düren/Maastricht, Germany, 2005.
52. Reinhold, B.; Naumann, J.; Spies, H.-J. Einfluß von Zusammensetzung und Bauteilgeometrie auf das Nitrierverhalten von Aluminiumlegierungen. *HTM J. Heat Treat. Mater.* **1998**, *53*, 329–336. [CrossRef]
53. Okumiya, M.; Tsunekawa, Y.; Murayama, T. Surface modification of aluminum using ion nitriding and fluidized bed. *Surf. Coat. Technol.* **2001**, *142–144*, 235–240. [CrossRef]
54. Clark, D.G.; Little, J.A.; Clyne, T.W. Ceramic/metal wetting in a spontaneous infiltration process for fabrication of metal matrix composites. In Proceedings of the International Conference on Advanced Composite Materials, Wollongong, Australia, 15–19 February 1993; pp. 993–999.
55. Minamino, Y.; Yamane, T.; Shimomura, A.; Shimada, M.; Koizumi, M.; Ogawa, N.; Takahashi, J.; Kimura, H. Effect of high pressure on interdiffusion in an Al-Mg alloy. *J. Mater. Sci.* **1983**, *18*, 2679–2687. [CrossRef]
56. Lumley, R.; Sercombe, T.; Schaffer, G. Surface oxide and the role of magnesium during the sintering of aluminum. *Metall. Mater. Trans. A* **1999**, *30*, 457–463. [CrossRef]
57. Wei, Z.; Shen, L.; Kuang, Y.; Wang, J.; Yang, G.; Lei, W. The evolution of preferred orientation and morphology of AlN films under various sputtering parameters. *J. Cryst. Growth* **2024**, *625*, 127439. [CrossRef]

Disclaimer/Publisher's Note: The statements, opinions and data contained in all publications are solely those of the individual author(s) and contributor(s) and not of MDPI and/or the editor(s). MDPI and/or the editor(s) disclaim responsibility for any injury to people or property resulting from any ideas, methods, instructions or products referred to in the content.